Optics Letters

Spatially multiplexed orbital-angular-momentum-encoded single photon and classical channels in a free-space optical communication link

Yongxiong Ren,[1,4,*] Cong Liu,[1] Kai Pang,[1] Jiapeng Zhao,[2] Yinwen Cao,[1] Guodong Xie,[1] Long Li,[1] Peicheng Liao,[1] Zhe Zhao,[1] Moshe Tur,[3] Robert W. Boyd,[2] and Alan E. Willner[1]

[1]Department of Electrical Engineering, University of Southern California, Los Angeles, California 90089, USA
[2]Department of Physics and Astronomy, The Institute of Optics, University of Rochester, Rochester, New York 14627, USA
[3]School of Electrical Engineering, Tel Aviv University, Ramat Aviv 69978, Israel
[4]Currently at FutureWei Technologies Inc., Santa Clara, California 95050, USA
*Corresponding author: yongxior@usc.edu

We experimentally demonstrate spatial multiplexing of an orbital angular momentum (OAM)-encoded quantum channel and a classical Gaussian beam with a different wavelength and orthogonal polarization. Data rates as large as 100 MHz are achieved by encoding on two different OAM states by employing a combination of independently modulated laser diodes and helical phase holograms. The influence of OAM mode spacing, encoding bandwidth, and interference from the co-propagating Gaussian beam on registered photon count rates and quantum bit error rates is investigated. Our results show that the deleterious effects of intermodal crosstalk effects on system performance become less important for OAM mode spacing $\Delta \geq 2$ (corresponding to a crosstalk value of less than –18.5 dB). The use of OAM domain can additionally offer at least 10.4 dB isolation besides that provided by wavelength and polarization, leading to a further suppression of interference from the classical channel.   © 2017 Optical Society of America

Quantum communication has become of increasing importance with the potential advances in information transfer and security [1–3]. In general, a quantum communication protocol employs a qubit system for encoding information, such as the polarization of a photon. Such systems can be easily implemented given that technology for encoding and decoding information in a qubit state-space is available, enabling system clock rates in the gigahertz (GHz) regime [4,5]. However, only one-bit information can be encoded on each photon for a qubit state.

It has been shown in a quantum system that employing multilevel quantum states for information encoding can help not only improve the photon efficiency but also increase the robustness against eavesdropping [6–8]. One example of enabling encoding by multilevel states is employing a set of orthogonal spatial modes for which the photon can occupy one of many states at a given time slot [8–10]. A possible spatial basis set that has recently received increasing interest is orbital angular momentum (OAM) modes [11]. A light beam with a helical wavefront carries an OAM corresponding to $\ell\hbar$ per photon, where $\hbar$ is the reduced Planck constant and ℓ is an unbounded integer [11]. OAM modes with different ℓ values are mutually orthogonal [12], which allows for the simultaneous transmission of multiple data channels [13,14]. Recent advances have shown the use of OAM modes for terabit/s classical optical links and for up to 143-km free-space transmission [13,15,16].

OAM states span a large Hilbert space and can be utilized for high-dimensional quantum encoding based on their orthogonality [10,17]. Moreover, quantum OAM encoding is in principle compatible with data encoding in other domains, such as polarization encoding [17,18]. A proof-of-concept OAM encoding-based quantum link has been recently demonstrated by using a digital micromirror device to switch between OAM states with a rate of 4 kHz limited by the switching device. 20 Gbit/s OAM encoding has been reported in the classical domain using a set of optical switches and fixed holograms [19]. A similar approach may also be applied to a quantum system to achieve a higher data encoding rate. In addition, a quantum channel may co-propagate with a classical channel in some systems [20–22]. In free-space quantum links, this classical Gaussian channel may act as a beacon for laser tracking or turbulence compensation subsystems, and could provide a public authenticated channel for key reconciliation [10,23]. Thus, it would be desirable to be able to distinguish the quantum signal from the classical one. In a non-OAM link, the quantum channel can be placed on a different wavelength or polarization [20,21]. For an OAM link, the use of OAM spatial modes for encoding can potentially further enhance the isolation between quantum and classical channels. As a result,
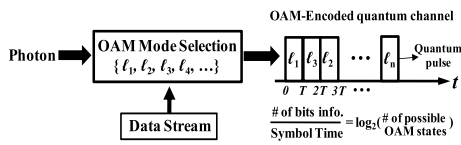
Fig. 1. Concept of quantum data encoding using OAM spatial modes. Within each symbol period, the OAM photon occupies one of n OAM states, resulting in a photon efficiency $\log_2(n)$ bits per photon.

the quantum signal could become more resistant to the interference from the classical channels.

In this Letter, we experimentally demonstrate an OAM-encoding-based free-space quantum link, in which the OAM-encoded photon is spatially multiplexed with a classical Gaussian beam located on a different wavelength and polarization and co-propagates in free space [24]. Data encoding on two OAM states is achieved with rates of 5–100 MHz by using a combination of two independently modulated laser diodes and two helical phase holograms. The dependence of system performance on mode spacing Δ and encoding rate is investigated. Our results show that intermodal crosstalk on system performance becomes negligible for $\Delta \geq 2$. We also explore the influence of the interference from the classical channel on an OAM quantum channel. It is found that the use of OAM states can provide at least 10.4 dB isolation between the multiplexed OAM photons and classical Gaussian beam besides that provided by wavelength and polarization.

Figure 1 illustrates the concept of data encoding using OAM states. Within each symbol period T, an OAM photon is placed in one possible of n OAM states. Compared to a qubit system based on polarization, this scheme could in principle increase the photon efficiency to $\log_2(n)$ bits per photon. The OAM photon is then spatially combined with a classical Gaussian channel and they co-propagate in free space. The classical channel is carried by a Gaussian beam with $\ell = 0$ that resides on a separate wavelength and on an orthogonal polarization.

Figure 2 shows the experimental setup. Two independent pseudorandom binary sequences with a symbol period of T produced by an arbitrary waveform generator are first amplified and then used to directly modulate two 850-nm laser diodes with single-mode fiber (SMF) pigtails. Tunable radio frequency and fiber delay lines are inserted into the paths so that the output signals of the two modulated lasers (branches ① and ②) are synchronized. The two signal beams are collimated in free space and then converted into two different OAM beams by using a programmable spatial light modulator (SLM-1). Depending on the spiral phase holograms loaded onto SLM-1, OAM beams

with different ℓ can be created, with beam sizes of 0.33, 0.39, 0.44, and 0.51 cm for $|\ell| = 1, 2, 3, 4$, respectively. These two OAM beams at λ_1 are then spatially combined using a beam splitter. The combined branches are attenuated to obtain weak coherent-state pulses, each containing an average photon number of μ. The quantum pulses are then spatially combined with an orthogonal polarized classical Gaussian beam at $\lambda_2 = 801.6$ nm using a polarizing beam splitter (PBS). The resulting multiplexed channels coaxially propagate ~1 meter in free space.

At the receiver, the multiplexed channels pass through another PBS and a free-space bandpass filter of λ_1 to separate out the quantum channel, with an isolation of 33 dB in polarization and of 71 dB in wavelength (104 dB in total), respectively. An SLM-based demultiplexer is then used to convert the OAM value ℓ into 0. This operation in the OAM domain can further enhance isolation between the OAM photon and the classical Gaussian beam. We note that the losses incurred by the polarization, wavelength, and OAM filtering would degrade system performance. The $\ell = 0$ photon of each branch is then coupled into an SMF and sent to a silicon avalanche photodiode (APD)-based single photon detector (SPD) operating in free-running mode. The SPDs have a deadtime of 50 ns, an after-pulsing probability of 0.5%, and dark counts of 500 counts per second. It would produce a 25-ns wide pulse when a photon event is detected. The two output signals of the SPDs are simultaneously sampled by a real-time scope at a sampling rate of 250-M samples/s and recorded for offline digital signal processing (DSP). The DSP procedure includes (i) removing detectable dark count events using a gating signal, (ii) identifying the transmitted OAM photon for each detected event, and (iii) mapping out the transmitted bit information and calculating the quantum bit error rate (QBER). Mathematically, the QBER in our system can be expressed as

$$QBER = \frac{\frac{1}{2}(2p_{\text{dark}} - p_{\text{dark}}^2) + 2p_{\text{opt}}p_{\text{phot}}}{2p_{\text{phot}} + 2p_{\text{dark}} - 2p_{\text{phot}}p_{\text{dark}}},$$

in which the numerator and denominator represent the probability of getting a false detection and the total probability of detection per pulse. $p_{\text{dark}} = n_{\text{dark}}\Delta\tau$, $p_{\text{phot}} = \frac{1}{2}\mu\eta_t\eta_d$, and p_{opt} denote the probabilities to get a dark count, to detect a photon for each branch, and that a photon enters into an erroneous detector, respectively [25]. n_{dark} is the dark count rate of the detector, and $\Delta\tau$ is the normalized detection time window with respect to pulse period. η_t and η_d are the channel transmission and detector efficiency ($\eta_t \cong 21\%$ and $\eta_d = 39\%$ at 850 nm in our experiment). p_{opt} can be determined by measuring the power transfer between two OAM states, i.e., intermodal
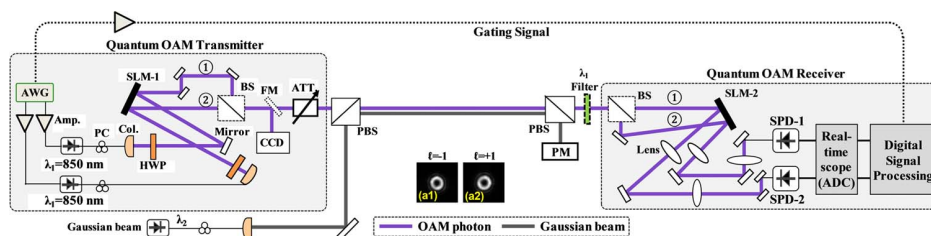
Fig. 2. Experimental setup of an OAM-based quantum link co-propagating with a classical Gaussian beam located on a different polarization and wavelength channel. ADC, analog-to-digital converter; Amp, amplifier; ATT, attenuation; AWG, arbitrary waveform generation; BS, beam splitter; Col, collimator; FM, flip mirror; HWP, half-wave plate; OC, optical coupler; PBS, polarizing beam splitter; PC, polarization controller; PM, power meter; SPD, single photon detector.

crosstalk. We can see that if OAM crosstalk is sufficiently low, system QBER is finally limited by the detector dark count rate as well as system transmission efficiency η_t and η_d.

Figure 3(a) presents the normalized waveforms for the outputs of the two laser diodes directly modulated at 10 MHz. The combined waveform verifies that light is routed to only one of the branches in each 100-ns period. Figure 3(b) depicts the received normalized waveforms after 25-dB attenuation, measured by an APD, when using mode sets $\ell = -1$ and $+1$ with $\Delta = 2$ (OAM crosstalk -18.5 dB). We see that only one OAM mode is active within each symbol period. The received waveforms of the two modes are well aligned in time by adjusting tunable delay lines. We note that in Fig. 3(b) the uneven region in the waveforms is mainly caused by the APD amplifier noise.

Figure 4(a) shows the normalized channel transfer matrices using both classical and quantum approaches. Each matrix element is measured as a ratio of the measured photon counts (power) to the maximum photon counts (power) in this matrix in a unit of dB. Due to crosstalk, dark counts, and noise, a photon in a particular OAM state $|\ell\rangle$ may be detected at the receiver in another OAM state $|\ell'\rangle$. For a lossless free-space transmission, we have $|\ell'\rangle = \mathbf{U}|\ell\rangle$, where $\mathbf{U}$ represents the propagation matrix and is unitary. $|\mathbf{UU}^*|$ can represent the power transfer matrix between OAM states. Significant photon counts are only registered for measurements of $\langle\ell' = i|\ell = i\rangle$ due to the orthogonality of OAM states, as shown in Fig. 4(a2). This is in good agreement with the classically measured matrix $|\mathbf{UU}^*|$ in Fig. 4(a1). Figure 4(b) depicts the single-photon measurements of the transfer matrices under different power levels of the Gaussian channel.

Figure 5 presents the registered photon counts per second for OAM state $\ell = +1$ and measured QBER curves of the OAM encoded link as a function of average photon number per received pulse μ when using mode sets $\{\ell = +1, +2\}$, $\{\ell = +1, -1\}$, and $\{\ell = +1, +4\}$. The intermodal crosstalk for these three cases are –12.7, –18.5, and –32.2 dB, respectively. As expected, the registered count rate increases with μ. For a fixed μ, smaller mode spacing Δ results in a larger count rate and a larger QBER due to crosstalk effects. We see that the QBERs tend to exhibit a slower decrease for the cases of $\Delta \geq 2$ when the influence of OAM crosstalk becomes negligible. At large μ and Δ, the QBER is mainly affected by the dark counts of SPDs and ambient light. Because of these, the minimum

achievable QBER measured in our link is around 6×10^{-3}. Figure 6 shows the measured QBER curves under different transmitted pulse rates. One can see that the cases of 5-M pulse/s and 10-M pulses/s show similar QBER performance for $\mu = 0.04$ to 4. However, the measured QBERs increase dramatically when pulse rates exceed 20 MHz due to the limited SPDs deadtime of 50 ns and increased after-pulsing events.

We also investigate the influence of the strength of the classical channel on the registered count rate and measured

(a) Without Gaussian channel

(a1) Classical |UU*|

Received ℓ_j \ Transmitted $|\ell_i\rangle$	0	1	2	3	4	5	6
0	-0.6	-22.7	-33.6	-33.6	-33.6	-33.6	-33.6
1	-13.2	-0.2	-14.9	-33.6	-33.6	-33.6	-33.6
2	-33.6	-15.1	-0.3	10.4	-23.7	-33.6	-33.6
3	-33.6	-33.6	-12.9	0	-8.7	-20.6	-33.6
4	-33.6	-33.6	-24.9	-10.4	-0.4	-7.8	-15.6
5	-33.6	-33.6	-30.6	-22.5	-9.2	-1.4	
6	-33.6	-33.6	-33.6	-33.6	-23.5	-8.3	-0.9

(a2) Quantum |UU*|

Received ℓ_j \ Transmitted $|\ell_i\rangle$	0	1	2	3	4	5	6
0	0	-21.2	-28.3	-27.1	-33.7	-33	-32
1	-10.4	0	-12.7	-25.6	-32.2	-28.1	-34.3
2	-28.1	-14.6	-0.8	8.6	-20.1	-24.8	-22.8
3	-32.1	-30.6		-0.7	-7	-18.7	-25
4	-32.7	-28.4	-22.1	-8.1	-1.13	-6.6	-15.1
5	-31.9	-33.1	-23.3	-20		-1.1	-6.7
6	-35.2	-34.4	-27.2	-26	-20.1		-1.6

(b) With Gaussian channel

(b1) Quantum |UU*| (72.2 dB)

Received ℓ_j \ Transmitted $|\ell_i\rangle$	0	1	2	3	4	5	6
0	0	-9.9	-13.1	-23.3	-23	-24.5	-24.3
1	-9	0.94		-16.1	-16.1	-18.6	-18.4
2	-10	-6.4	-0.29	-6.9	-11.9	-15.3	-14.6
3	11.7	-9.3		-0.07		-12.7	-12.6
4	12.2	-12.1	-12.2		-0.65	7.6	-9.9
5	-18.4	-18.9	-18.5	-18.2		-0.44	
6	24.3	-24.5	-24.5	-23.1	-22.4		-0.27

(b2) Quantum |UU*| (80.7 dB)

Received ℓ_j \ Transmitted $|\ell_i\rangle$	0	1	2	3	4	5	6
0	0	-3.17	-10.9	-15.4	-15	-16.7	-17
1	-2.68	-0.44	-3.92	-10.8	-12.9	-13.5	-16.8
2	3.32	-2.92	-0.11		-10	-12.7	-12.8
3	-6.7	-6.6		-1.14		6.2	10.3
4	11.9	-12	-11.4		-0.84	-6	-6.5
5	16.8	-16.8	-16.3	-14.2		-0.74	
6	-17	-17	-16.2	-12.5	-12.7		-0.36

Fig. 4. (a) Channel transfer matrices from $\ell = 0$ to $\ell = +6$ using classical (a1) and quantum (a2) measurement approaches. (b) Quantum transfer matrices under the influence of the Gaussian channel. The power of the received Gaussian beam is 80.7 dB and 72.2 dB higher than that of the OAM photon.
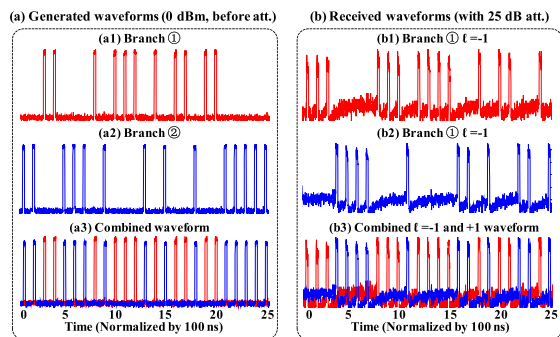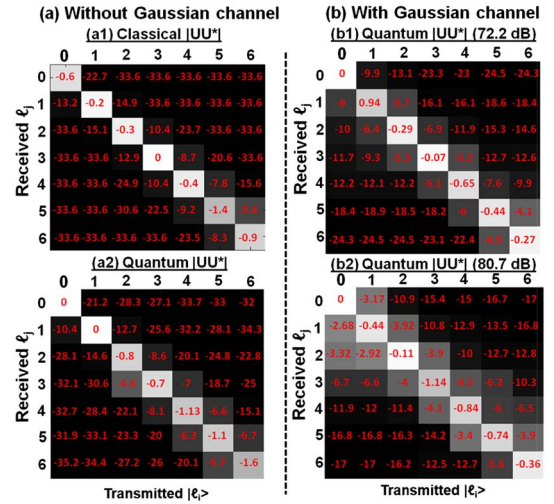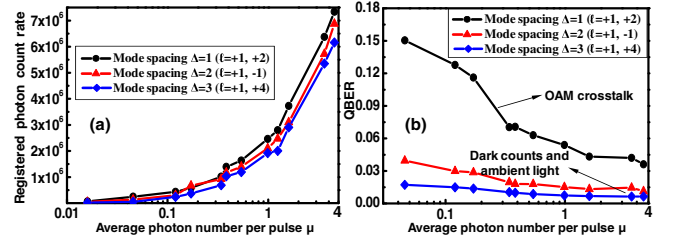
Fig. 3. (a) Normalized waveforms of the two branches (a1–a2) and their combination (a3), generated by directly modulated laser diodes. (b) Received waveforms of the two branches (b1–b2) and their combination after 25-dB attenuation (b3) when using mode set $\{\ell = -1, +1\}$ with $\Delta = 2$. The symbol period is 100 ns.

Fig. 5. (a) Registered photon count rate and (b) measured QBERs for different mode spacing ($\Delta = 1$, 2, and 3) as a function of average photon number per received pulse.
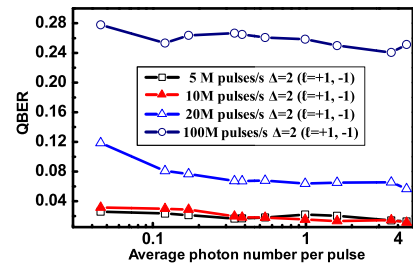
Fig. 6. Measured QBERs under various transmitted pulse rates (5 M, 10 M, 20 M, and 100 M pulses/s) as a function of average photon number per received pulse.
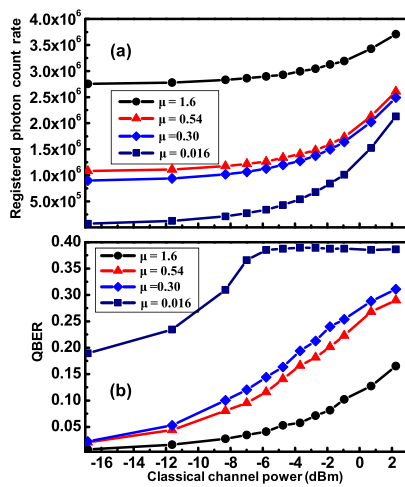
Fig. 7. (a) Registered photon count rate and (b) measured QBERs as a function of classical channel power under different average photon numbers of the OAM photon.

QBERs. Figure 7 presents the registered count rate and QBERs as a function of power levels of the classical channel when using mode sets $\ell = -1$ and $+1$ at 10 MHz. As can be found from the channel transfer matrix in Fig. 4(a), the crosstalk onto neighbored OAM modes when only sending a Gaussian channel is less than −10.4 dB. This indicates that the OAM domain can further allow for at least 10.4 dB separation from the classical channel in addition to 104 dB provided by wavelength and polarization. We see that the registered photon count rate increases rapidly as the power of the classical channel exceeds a threshold, corresponding to a normalized power of −16 dB with respect to the OAM photon. The measured QBERs are above 0.1 when the classical channel power is larger than −8.2, −7.1, and −1.0 dBm under an average photon number μ of 0.30, 0.54, and 1.6, respectively. We note that the high QBERs for $\mu = 0.016$ mainly result from the dark count effects.

We experimentally demonstrate spatial multiplexing of an OAM-encoded quantum channel and a classical Gaussian beam. We investigate various system performance dependences, such as mode spacing, encoding rate, and classical channel interference. When considering the two OAM states and 10s MHz rate shown in this Letter, we believe that our experiment could be potentially scaled to a larger number of OAM states at a higher encoding rate. Since our laser diodes have a modulation bandwidth of about 1 GHz, the OAM photon can be encoded at GHz at the transmitter. The MHz-level encoding rate in our experiment is mainly constrained by the deadtime of the receiver SPD array. Moreover, for a practical system, the number of accommodated OAM states is generally limited by various factors, including hardware complexity, intermodal crosstalk, aperture sizes, and channel condition [23].

REFERENCES

1. N. Gisin, G. Ribordy, W. Tittel, and H. Zbinden, Rev. Mod. Phys. **74**, 145 (2002).
2. C. Bennett and G. Brassard, in *International Conference on Computers, Systems & Signal Processing*, Bangalore, India (1984), pp. 175.
3. H. Takenaka, A. Carrasco-Casado, M. Fujiwara, M. Kitamura, M. Sasaki, and M. Toyoshima, Nat. Photonics **11**, 502 (2017).
4. H. Takesue, S. W. Nam, Q. Zhang, R. H. Hadfield, T. Honjo, K. Tamaki, and Y. Yamamoto, Nat. Photonics **1**, 343 (2007).
5. N. Namekata, H. Takesue, T. Honjo, Y. Tokura, and S. Inoue, Opt. Express **19**, 10632 (2011).
6. H. Bechmann-Pasquinucci and W. Tittel, Phys. Rev. A **61**, 062308 (2000).
7. N. J. Cerf, M. Bourennane, A. Karlsson, and N. Gisin, Phys. Rev. Lett. **88**, 127902 (2002).
8. G. Vallone, V. D'Ambrosio, A. Sponselli, S. Slussarenko, L. Marrucci, F. Sciarrino, and P. Villoresi, Phys. Rev. Lett. **113**, 060503 (2014).
9. A. Mair, A. Vaziri, G. Weihs, and A. Zeilinger, Nature **412**, 313 (2001).
10. M. Mirhosseini, O. S. Magaña-Loaiza, M. N. O'Sullivan, B. Rodenburg, M. Malik, M. P. J. Lavery, M. J. Padgett, D. J. Gauthier, and R. W. Boyd, New J. Phys. **17**, 033033 (2015).
11. L. Allen, M. W. Beijersbergen, R. J. C. Spreeuw, and J. P. Woerdman, Phys. Rev. A **45**, 8185 (1992).
12. G. Gibson, J. Courtial, M. Padgett, M. Vasnetsov, V. Pas'ko, S. Barnett, and S. Franke-Arnold, Opt. Express **12**, 5448 (2004).
13. J. Wang, J.-Y. Yang, I. M. Fazal, N. Ahmed, Y. Yan, H. Huang, Y. Ren, Y. Yue, S. Dolinar, M. Tur, and A. E. Willner, Nat. Photonics **6**, 488 (2012).
14. M. Krenn, R. Fickler, M. Fink, J. Handsteiner, M. Malik, T. Scheidl, R. Ursin, and A. Zeilinger, New J. Phys. **16**, 113028 (2014).
15. M. Krenn, J. Handsteinera, M. Fink, R. Fickler, R. Ursin, M. Malik, and A. Zeilinger, Proc. Natl. Acad. Sci. USA **113**, 13648 (2016).
16. Y. Ren, Z. Wang, P. Liao, L. Li, G. Xie, H. Huang, Z. Zhao, Y. Yan, N. Ahmed, A. Willner, M. P. J. Lavery, N. Ashrafi, S. Ashrafi, R. Bock, M. Tur, I. B. Djordjevic, M. A. Neifeld, and A. E. Willner, Opt. Lett. **41**, 622 (2016).
17. A. Sit, F. Bouchard, R. Fickler, J. Gagnon-Bischoff, H. Larocque, K. Heshami, D. Elser, C. Peuntinger, K. Günthner, B. Heim, C. Marquardt, G. Leuchs, R. W. Boyd, and E. Karimi, Optica **4**, 1006 (2017).
18. Z. Qu and I. B. Djordjevic, Opt. Express **25**, 7919 (2017).
19. A. J. Willner, Y. Ren, G. Xie, Z. Zhao, Y. Cao, L. Li, N. Ahmed, Z. Wang, Y. Yan, P. Liao, C. Liu, M. Mirhosseini, R. W. Boyd, M. Tur, and A. E. Willner, Opt. Lett. **40**, 5810 (2015).
20. N. A. Peters, P. Toliver, T. E. Chapuran, R. J. Runser, S. R. McNown, C. G. Peterson, D. Rosenberg, N. Dallmann, R. J. Hughes, K. P. McCabe, J. E. Nordholt, and K. T. Tyagi, New J. Phys. **11**, 045012 (2009).
21. T. J. Xia, D. Z. Chen, G. Wellbrock, A. Zavriyev, A. C. Beal, and K. M. Lee, in *Optical Fiber Communication Conference* (2006), paper OTuJ7.
22. J. Carpenter, C. Xiong, M. J. Collins, J. Li, T. F. Krauss, B. J. Eggleton, A. S. Clark, and J. Schröder, Opt. Express **21**, 28794 (2013).
23. Y. Ren, G. Xie, H. Huang, C. Bao, Y. Yan, N. Ahmed, M. P. J. Lavery, B. I. Erkmen, S. Dolinar, M. Tur, M. A. Neifeld, M. J. Padgett, R. W. Boyd, J. H. Shapiro, and A. E. Willner, Opt. Lett. **39**, 2845 (2014).
24. Y. Ren, C. Liu, K. Pang, J. Zhao, Y. Cao, G. Xie, L. Li, Z. Zhao, Z. Wang, M. Tur, R. Boyd, and A. E. Willner, in *Conference on Lasers and Electro-Optics* (2017), paper SW4I.4.
25. H. Zbinden, H. Bechmann-Pasquinucci, N. Gisin, and G. Ribordy, Appl. Phys. B **67**, 743 (1998).